Research

Author for correspondence:
R. A. Palmer
e-mail: ryan.palmer@bristol.ac.uk

THE ROYAL SOCIETY
PUBLISHING

The role of body shape and mass in skimming on water

R. A. Palmer[1] and F. T. Smith[2]

[1]School of Mathematics, Fry Building, Woodland Road, Bristol BS8 1UG, UK
[2]Department of Mathematics, University College London, London WC1H 0AY, UK

RAP, 0000-0001-8964-9014; FTS, 0000-0003-4850-995X

Over many years, there has been great practical interest in how solid bodies interact with and skim on liquid layers. In the present investigation, the focus is on the important role of body mass and shape in such skimming motions. Considering a thin two-dimensional solid body that impacts obliquely and then rebounds on a shallow inviscid water layer, we develop a mathematical model to predict quantitatively the duration and evolution of the body and fluid motions and indeed the success or failure of the whole skim. In the current setting, the shallow water layer thickness is small relative to the representative body length. The combined roles of increased mass and shape are found to be crucial, governed by a similarity solution. The relationship $C \sim M^{2/3}$ between scaled body curvature and mass is identified and highlighted. In particular, increased convex curvature of the underbody is found to alter the interactive pressure in such a way that it inhibits the occurrence of a super-elastic response in the exit vertical velocity and height of the body, and in effect enables a much heavier body to skim successfully provided the above relationship is maintained.

1. Introduction

The skimming of a thin body, i.e. the low-angle impact of a body onto water and its subsequent exit, has both playful and serious interests behind it. The playful aspect is very well-known to many people through their efforts at skimming a slender stone across a stretch of water. The serious aspect, on the other hand, which is perhaps
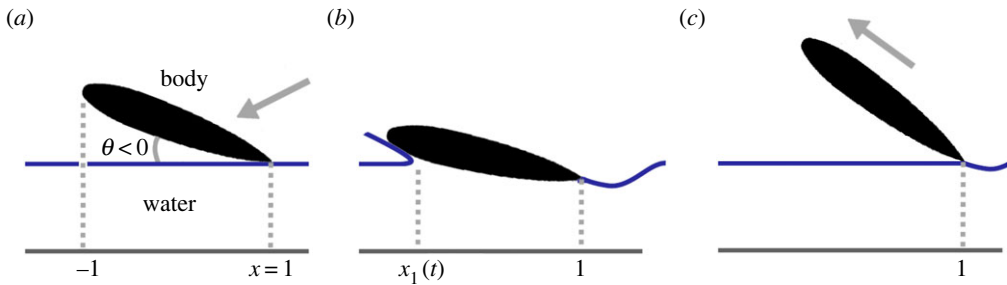
Figure 1. Illustrative (non-dimensional) sketch of a successful skimming motion for a curved body of large mass. The sub-figures show successive points within the body motion: (*a*) body entry, (*b*) mid-skim and (*c*) exit (rebound). The combined effects of increased body mass and underbody shaping are investigated in the paper. (Online version in colour.)

less well-known and potentially more worthy of quantification, concerns various applications in industry and aviation. These include icing-impact applications on aircraft surfaces [1–4], the repeated bouncing of meteors and the landing of aeroplanes on water [5–7].

The present study is on the skimming of a two-dimensional thin body on a shallow layer of inviscid water or other liquid but with particular attention paid to the influence of body shape and weight as an important new aspect. Experienced stone throwers are well aware of the crucial role that stone shape and weight play in skimming a stone across water. However, the main practical motivation of our study comes from repeated particle-skimming over water layers on vehicle surfaces as a safety issue [1–4], where the particles can take many distinct sizes and shapes. Substantial heat transfer is often generated when such skimming takes place with ice particles. The main research aim here is to understand and quantify physically how bodies that are both relatively thick and heavy can skim, where thickness may be associated with underbody curvature and heaviness with the body mass.

For shallow-water skimming, the Hicks & Smith [8] model describes the dynamic fluid/body interaction involved when the body motion is driven by the pressure force due to the disturbed water flow acting between the underbody and the horizontal substrate, with the effects of air flow being negligible during contact with the water. Subsequently, however, between-skim air flow effects were accounted for by Liu & Smith [9] in their consideration of multiple skims with weight rather than mass affecting the body motion between successive skims. Flat underbody shapes are the prime concern in the above works, whereas curved shape effects are included by Palmer & Smith [10]. Our focus here is on the combined role of shape and mass since they both tend to be present and important in practice, and there is much interest in their joint influence on the success (rebound) or failure (flooding) of the skim, especially in realistic cases where both the shape variation (e.g. curvature) and the mass are increased in magnitude. Thus, we seek to understand the conditions under which heavier bodies may skim successfully rather than flood and sink, presenting new practical dangers (e.g. new dynamics to consider in aircraft icing).

Figure 1 illustrates a successful skimming motion for a curved body of significantly large mass, as is modelled in this paper. Each of the sub-figures shows a successive point within the body motion, in the body frame. The body has an overall length of 2 through its centre (notably the angles of incidence are accentuated in these sketches). During the skimming motion the body undergoes a vertical translation and body rotation about the trailing edge ($x = 1$). The leading contact point between the body and the water layer, $x_1(t)$ is unknown and the corresponding wetted region extends from the trailing edge to this point, along the underbody, during the middle of the skim, (*b*). A so-called super-elastic response is depicted in (*c*), whereby a body of large mass rebounds and exits the water layer at a greater height and vertical velocity than its entry (*a*): the greater height and vertical velocity here essentially define the term super-elastic. This phenomenon is explained further in the analysis to follow.

Concerning the leading contact point $x_1(t)$, whose position is unknown, the flow can reverse upstream of this point, potentially producing a thin splash jet extending ahead of the body. A small so-called 'square' Euler region encompasses the leading contact position, continuing to surround it as it moves, and the Euler region where flow angles become $O(1)$ describes the liquid layer turnover. These effects are incorporated into the modelling via pressure jump conditions [8,11]. Importantly, however, upstream of this region the oncoming water layer is undisturbed to leading order. Another point for consideration is the contact angle between the liquid layer and the body (the angle between the free surface and underbody, at the point where the free surface detaches from the body). In describing the body motion via the leading contact point (as above), the possibility for a splash jet to form, and the linearized theory (detailed below), the location where the liquid layer detaches from the body is unknown. However, the precise dynamics of the fluid–body interaction inside the small Euler region at this point are not required to capture the body's skimming motion to leading order and therefore are not explicitly modelled.

The typical skim here is for oblique impact involving small angles of body incidence and small angles in the induced water flow direction, with the trailing edge of the two-dimensional body impacting first. This initial point of contact tends to lead to the expectation that separation or detachment will continue to be subsequently situated at the trailing edge, although different detachment sites are certainly possible [12,13] following other forms of initial impact. The flow is reasonably assumed to be unsteady, incompressible, inviscid and two-dimensional. In the body frame the Hicks & Smith [8] model applies based on shallow-water balances beneath the underbody for small perturbations about the oncoming uniform flow; this is coupled with Newton's laws for the body motion, yielding two-way interaction. It should be remarked that there is a considerable and notable literature on impacts generally, for example [5–12,14–27], covering parameter ranges which tend to be quite different from the present. Among these studies are a variety of configurations that consider impact onto deep water, including: the early and pioneering works that focus on the landing of seaplanes [5,6,14]; and the mathematical treatment of different shaped skimmers/bouncers, including flat plates [7,15,16], wedges [19], cylinders [20], ellipses [12] and spheres [25]. Further recent and notable works include [22,23,25–27] which cover a range of new physical considerations (such as tangential velocities [23] and droplet impacts [27]). For a full discussion of many of these papers, we refer interested readers to the original work of Hicks & Smith [8].

A significant difference in the present work is the water being shallow, with a water layer depth much less than the body length; an additional difference is that our work has the body being free to move subject to the forces acting on its surface because of the unknown fluid dynamics, thus yielding two-way fluid/body coupling. Altogether, with the variations in the underbody shape significantly smaller than the liquid-layer thickness, the current study lies in a regime between the theories of Tuck & Dixon [11] and Korobkin [22] and that of Wagner [6]. Of note, many of the other regimes examined above present a range of different physics and therefore require other considerations and assumptions. For instance, several recent experimental and modelling studies contrast with the present work by studying low Weber number interactions in deep water baths in which capillary effects become important, e.g. [25–27].

The mathematical model is presented in §2 which describes the relevant physical scales of the skim including those of the body shape, represented by thickness or underbody curvature, and the body mass, as well as presenting the perturbed water flow and the nonlinear interactive system. For example, the representative time scale of a successful skim is usually somewhat short, being of order L_D/U_D where L_D and U_D are the typical body half-length and incident speed, respectively, in dimensional (D) terms. Thus, a stone of representative length 5 cm and speed of order $10\,\mathrm{ms}^{-1}$ yields a time scale of order 0.005 s, while a small particle say of length 5 mm impacting on a vehicle at $50\,\mathrm{ms}^{-1}$ yields a scale of order 0.0001 s. In the context of aircraft landing on water, the typical speed of approach for an aeroplane is approximately $50\,\mathrm{ms}^{-1}$, landing on 10 m floats and giving a time scale of 0.2 s. The vertical velocity component which is necessary for an impact is implied by the range of small approach angles of the thin body. Section 3

gives numerical solutions of the nonlinear integro-differential system when shaping and mass are varied. The metrics of interest include: contact time (duration of skim), penetration depth (extent of body wetting and height of centre of mass), body moment, leading edge pressure and wake profiles. Then §4 addresses emerging analytical properties as shaping and mass increase. A crucial relation, $C = O(M^{2/3})$, is found between the scaled curvature C and mass M for the success of a skim for a relatively heavy body. Conclusions are provided in §5 along with comments on more nonlinear effects and further discussion.

2. The skimming model

The body of mass m_D and length $2L_D$ is thin and impacts on the water obliquely at a small angle with horizontal velocity U_D, as in [8]. The development of the physical model and governing equations follows that of Hicks & Smith [8]. Interested readers are encouraged to see their derivation for further details. Our purpose here is to build upon this study and several others [9,10,13,28] by investigating the unexplored combined effects of underbody curvature and mass, producing new physical insights through numerical and analytical investigations of such skimming body interactions and showing the dominant underlying physics at different stages of the skimming motion.

In the body frame, i.e. relative to the centre of mass, non-dimensional Cartesian coordinates $(x, \epsilon y)$ are measured with respect to L_D, where the small constant ϵ represents the typical angles involved, and the freely moving underbody surface $y = h$ can then be described by

$$h(x,t) = Y(t) + x\theta(t) - T(x). \tag{2.1}$$

Here, time is $U_D t / L_D$, $T(x)$ is the fixed shape of the underbody, θ is the scaled rotation angle and Y denotes the perturbation height of the centre of mass, which lies at the mid-point $x = 0$ in the present cases. The leading and trailing edges of the body are at $x = -1, x = 1$, respectively. The governing equations and conditions presented below form the basis for the numerical and analytical investigations in subsequent sections.

During the skim, only the pressured or 'wetted' underbody is subjected to the excess pressure of the water flow beneath, while the remainder of the body surface is subjected to atmospheric pressure (taken as zero without loss of generality). The surrounding atmosphere, typically air, is thus treated as a void whose dynamics has a negligible effect during the skim. In practice air cushioning as in [29–32] could be significant; as yet no rational means of incorporating air cushioning into a skim model has been found but we should mention in passing that research by FTS with Ellen Jolley is underway. In the current model, if $x = x_1(t)$ is the moving contact point at the front of the wetted underbody at time t then the body motion is described by

$$MY'' = \int_{x_1}^{1} p(x,t)\, \mathrm{d}x \tag{2.2a}$$

and

$$I\theta'' = \int_{x_1}^{1} x p(x,t)\, \mathrm{d}x, \tag{2.2b}$$

which account for the vertical and rotation motions. Here, the pressure is $\rho_D U_D^2 p$ with ρ_D being the water density, while M, I denote the scaled mass and moment of inertia given by $m_D \epsilon / (\rho_D L_D^2), I_D \epsilon / (\rho_D L_D^4)$ in turn. For the time scales of interest, the body's horizontal motion in the laboratory frame consists of a constant x-wise velocity of unity in scaled terms, since the horizontal forces on the thin body are relatively small, and this then supports the fixed-origin assumption in the body frame used in the present work.

The water flow is modelled as free of viscous, gravity and capillary effects because of the large typical Reynolds, Froude and Weber numbers (e.g. for a 5 cm stone travelling at a speed of $10\,\mathrm{ms}^{-1}$ on a water layer: $Re \sim 75\,000, Fr \sim 200, We \sim 67\,000$, or for a 5 mm particle at a speed of $50\,\mathrm{ms}^{-1}$: $Re \sim 190\,000, Fr \sim 51\,000, We \sim 170\,000$) and therefore shallow water equations apply in

Table 1. Table parameters for the numerical investigations.

parameter	value
perturbation height of centre of mass, Y_0	$4 + 2C$
vertical velocity of the body, V_0	-1
scaled angle of body rotation, θ_0	$-4 - 2C$
angular velocity of the body, ω_0	0
scaled body mass, $M = 3I$	scaled moment of inertia, $I = 1, 2, 3, 4$

the small-perturbation form

$$h_t + h_x + u_x = 0 \tag{2.3a}$$

and

$$u_t + u_x = -p_x, \tag{2.3b}$$

when $x_1(t) < x < 1$. These balances concern the kinematic condition and the horizontal momentum of the water flow, respectively, with the perturbation water velocity $u(x, t)$ and pressure $p(x, t)$ independent of y due to the uniform oncoming flow and the vertical momentum. The perturbation height h here is measured with respect to the undisturbed water level. In the wake region $x > 1$, the pressure is constant (atmospheric) and so $p(1, t) = 0$ such that

$$h_t + h_x + u_x = 0 \tag{2.4a}$$

and

$$u_t + u_x = 0, \tag{2.4b}$$

giving the water velocity and free-surface height aft of the body.

The conditions holding at the contact point allow for local conservation of mass and momentum, as a thin splash jet is generated locally, yielding

$$p + (1 - x_1')u = 0 \quad \text{at } x = x_1^+ \tag{2.5a}$$

and

$$u + (1 - x_1')h = 0 \quad \text{at } x = x_1^+, \tag{2.5b}$$

where the prime denotes differentiation in time. Finally, here the condition

$$p = 0 \quad \text{at } x = 1 \tag{2.6}$$

stems from the Kutta requirement at the trailing edge.

The body motion and the water flow, along with other responses, and indeed the success or failure of the skim, depend as in Hicks & Smith [8] on the solution properties of the nonlinear system (2.1)–(2.6) for h, u, p, Y, θ, x_1, given that initially h is zero and x_1 is unity at time zero. Further comments on nonlinear influences will be made later. The modelling, equations and method follow the derivation of [8]; however, the analysis is now extended to study the effects of the prescribed underbody shape $T(x)$ and the mass M (with the moment of inertia I remaining proportional to M in practice). The influence of the relationship between the typical thickness size $|T|$ and the mass is to be investigated below (§3, 4) as they are varied (the parameters used for our analysis below are shown in table 1).

3. Computational solutions

The stress in this section is on numerical solutions and their properties for $O(1)$ values of the parameters present. To maintain the physicality of the model, the initial touchdown must occur at the trailing edge which is required to remain fixed at $x = 1$ throughout the skimming motion. Furthermore, we require that the body makes contact with the liquid layer over a single region.

Clearly, $x = 1$ must be a simple root of $T(x)$ with the underbody thickness function satisfying $T(1) = T(-1) = 0$. Thus

$$T(x) = (1-x)\left(\sum_{m=0}^{n-1} a_m x^m\right), \quad \sum_{m=0}^{n-1} a_m(-1)^m = 0, \tag{3.1}$$

where the a_m constants are known. If $n = 1$ then $T(x) = 0$, giving a flat plate. By contrast, cases where $n = 2, 3, \ldots$ are addressed below (here and §4) since these correspond to a curved body.

To calculate the motion of the body through the water layer, specifically the fluid flow and body responses in the wetted region $[x_1, 1]$, we obtained computational solutions using a seventh- and eighth-order Runge–Kutta integration. This was with an adaptive step size [33] initiated by applying the small-time conditions set out in [8,10]. The code is an adaptation of a freely and openly available solver [34], which has been edited to solve a linear system of equations at each time step (the code is available online as part of the current paper's electronic supplementary material). The contact point $x_1(t)$ is determined as part of the numerical scheme, full details of which are given in [8,10,33].

In all of the computational results in this section, we consider a quadratic underbody shape

$$T(x) = C(1 - x^2). \tag{3.2}$$

Here, C is the scaled curvature of the underbody. Our main interest is in the influences of M, I and C on the overall dynamics of the skimming motion and in determining either the successful rebound of the body (where the wetted region remains within the confines of the body's length throughout the skim, i.e. $-1 \le x_1 < 1$) or failure due to flooding (where fluid is able to run over the top of the body [35], i.e. $x_1 < -1$ at some point during the skimming motion).

To begin the exploration of the solution properties for $O(1)$ parameter values, we discuss in (a) below the fundamental characteristics of the skimming interaction, following the three stage structure from the analysis in §4. After that, in (b), we highlight solution trends as mass M and thickness effect C increase with I proportional to M throughout.

(a) The general skimming motion

To explain the entire skimming motion, we provide four figures to be considered together. In figure 2, the change in the leading contact position x_1 throughout the skim(s) is displayed, in figures 3 and 4, the body's vertical motion and rotational behaviour are shown respectively, and finally in figure 5 the contact-point pressure at x_1 is presented.

(i) Stage 1: water entry

The skimming motion is initiated at the trailing edge of the body where it makes first contact with the water layer ($x = 1$, in figures 1 and 2). Since the body has an initial negative vertical velocity (V in figure 3), the body descends into the water ($Y - Y_0$ initially falls linearly in figure 3), forming a region of contact between the body and the water that extends from the fixed trailing edge, along the underbody, to the leading contact position ($x_1(t)$).

(ii) Stage 2: the majority of the skimming motion

As the body continues to descend, the size of the wetted region grows with x_1 moving towards the body's leading edge ($x = -1$). However, throughout this descent, the pressure on the underbody increases as the water resists the body's motion (figure 5), decreasing its velocity and causing the body to rotate in an anti-clockwise direction ($\omega > 0$, figure 4), thus reducing the body's angle of incidence ($\theta - \theta_0 > 0$, figure 4).

At some point during the skim, the wetted region reaches a maximum size, for which two cases are possible. Firstly, as previously noted, when the body's mass is too large compared to the curvature (as shown in figure 2) the wetted region may extend to and pass the body's leading edge such that $x_1 < -1$ in effect. This represents the onset of flooding and the body may
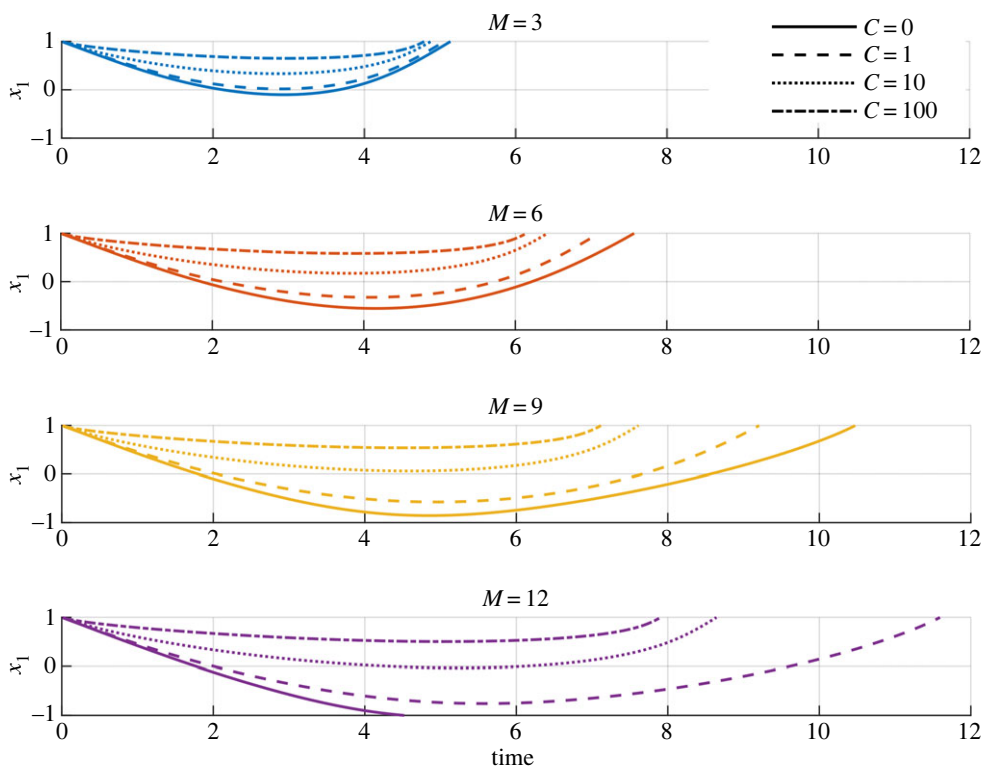
Figure 2. Evolution of contact point x_1 as a function of scaled time for varying $M = 3I$, with $I = 1, 2, 3, 4$, and varying $C = 0, 1, 10, 100$. See table 1 for all parameter values. (Online version in colour.)

sink soon afterwards. When this occurs we no longer consider the body's subsequent motion (see the case where $M = 12$ and $C = 0$ in figure 2). In this instance, the pressure under the body has not grown large enough to reverse its downward trajectory and thus the body fails to move upwards.

Secondly, however, if M and I are not too large compared with C (for the given initial conditions) then $x_1(t) > -1$ throughout the entire skimming motion, and a rebound occurs. At a particular time during the skimming motion, the vertical velocity becomes positive and the body begins to ascend through the water layer with the wetted region beginning to shrink (as depicted by the leading contact position moving back towards $x = 1$). Throughout this process, the pressure under the body reaches a peak and also begins to fall towards zero while (in most cases) the body continues to rotate in an anti-clockwise fashion.

(iii) Stage 3: water exit

When the above drop in pressure occurs the body is close to exiting the water layer. While the leading contact point gets closer to the trailing edge the pressure rapidly tends to zero [8]. This causes the body's vertical and angular velocities to tend to a near constant over a short time period. When $x_1(t_e) = 1$, at some exit time t_e, the body leaves the water layer at a height $Y(t_e)$ with an angular inclination of $\theta(t_e)$. These values will then determine the body's subsequent flight through the air; this air flight is not considered here.

While the above description is true in general, some very interesting dynamics can occur when different values of body mass (M), moment of inertia (I) and underbody curvature (C) are considered, which we proceed to do next.
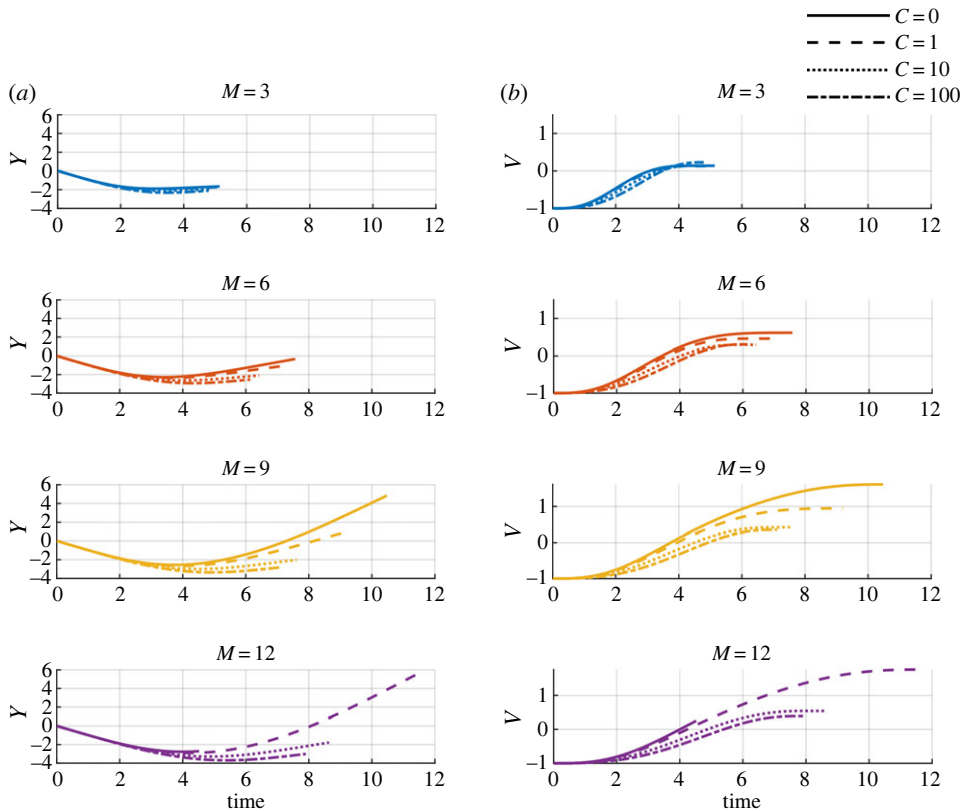
Figure 3. (*a*) Evolution of centre of mass height Y as a function of scaled time. (*b*) Evolution of vertical velocity V as a function of scaled time. Each plot is for varying $M = 3I$, $I = 1, 2, 3, 4$, and varying $C = 0, 1, 10, 100$. See table 1 for all parameter values. (Online version in colour.)

(b) The effect of increased underbody curvature on a heavy-body skim

(i) Duration of skimming motion

The size of M and I relative to C affects the duration of the skim and thus the magnitude of body wetting (e.g. the minimum value of x_1). For a flat body ($C = 0$) or cases of comparatively small C relative to M and I (e.g. $C = 1$) the duration of the skim increases with M and I as does the amount of body wetting. However, when C increases there is a significant influence from the underbody curvature on the body trajectory leading to shallower water penetration, a reduction in skimming duration towards a limit and a more rapid exit. Notably, when $M = 12$ the flat-body floods but increased curvature prevents this from occurring such that curved, heavier bodies are able to sustain full skimming motions that would otherwise flood or potentially sink equivalent flatter bodies.

(ii) Qualitative change in underbody pressure

The variation in body wetting is largely accounted for by the qualitative change in underbody pressure that occurs with increased C. When the body's mass is smaller, a larger value of body curvature results in a greater magnitude of pressure throughout the skimming motion. Yet, when the body begins to ascend through the water the pressure also reduces more quickly, a phenomenon which is associated with the body's more rapid exit. On the other hand, when we consider the largest values of M and I, if C is relatively small, the overall shape of the pressure
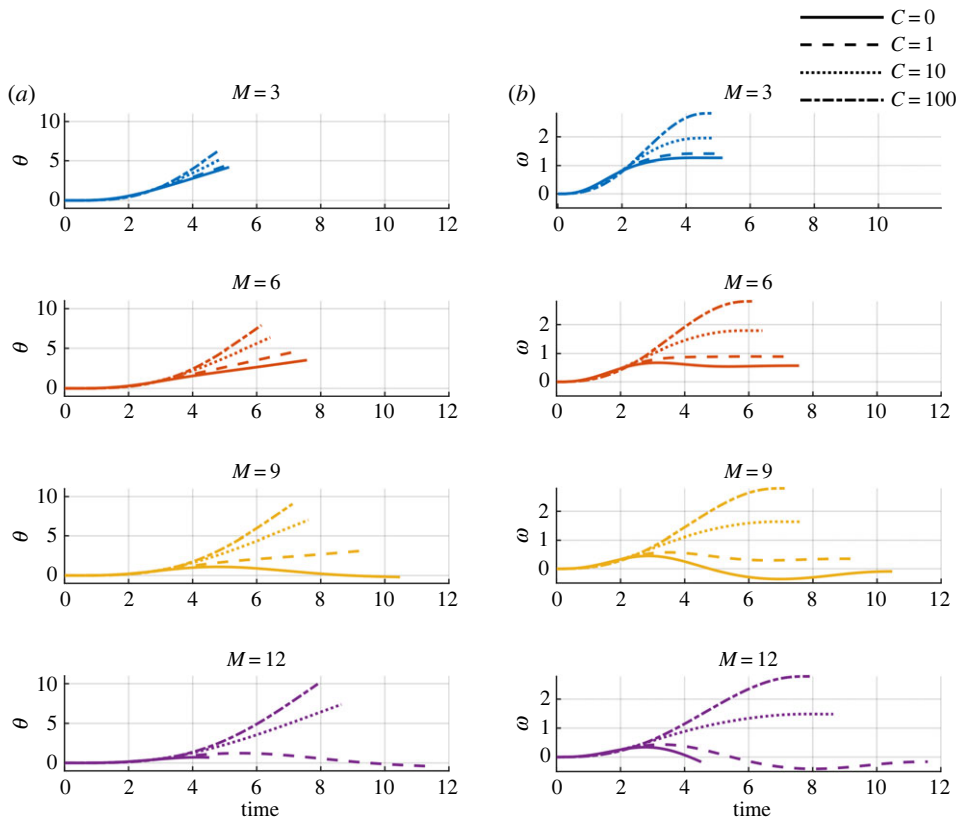
9

royalsocietypublishing.org/journal/rspa   Proc. R. Soc. A **479**: 20220311

Figure 4. (*a*) Evolution of scaled angle of rotation θ as a function of scaled time. (*b*) Evolution of angular velocity ω as a function of scaled time. Each plot is for varying $M = 3I$, $I = 1, 2, 3, 4$, and varying $C = 0, 1, 10, 100$. See table 1 for all parameter values. (Online version in colour.)

curve changes with a higher pressure sustained for longer towards body exit (for comparative values of C). By increasing C, this trend is counteracted, indicating that there is a value of C relative to M and I at which the influence of body curvature on the skimming dynamics overtakes those of the mass and moment of inertia (e.g. compare the curve of $C = 0$ with those for the other C values when $M = 9$).

(iii) Inhibition of vertical motion

The body's vertical motion changes dramatically with increased M and I; however, larger values of C are shown to inhibit this (figure 3). In detail, when M and I are comparatively small relative to the body curvature, the body leaves the water at a lower height than it entered with a smaller magnitude of vertical velocity ($Y - Y_0 < 0$ and $V < V(0) = 1$ in figure 3). Yet, when M and I increase and C remains small a so-called 'super-elastic response' is possible which has remarkably different characteristics. In particular, the body is able to leave the water layer with far greater vertical velocity and at a greater height than it entered with. This curious response is a result of the body's angle of inclination and a developing splash jet under the body working to convert a proportion of the water's large horizontal kinetic energy into vertical kinetic energy that propels the body out of the water layer. It is found however that with increased C this super-elastic response is inhibited both in terms of velocity and the exit height of the body. For an example of this see the case for $M = 9$ in figure 3 as C increases (a result of the change in the pressure profile under the body).
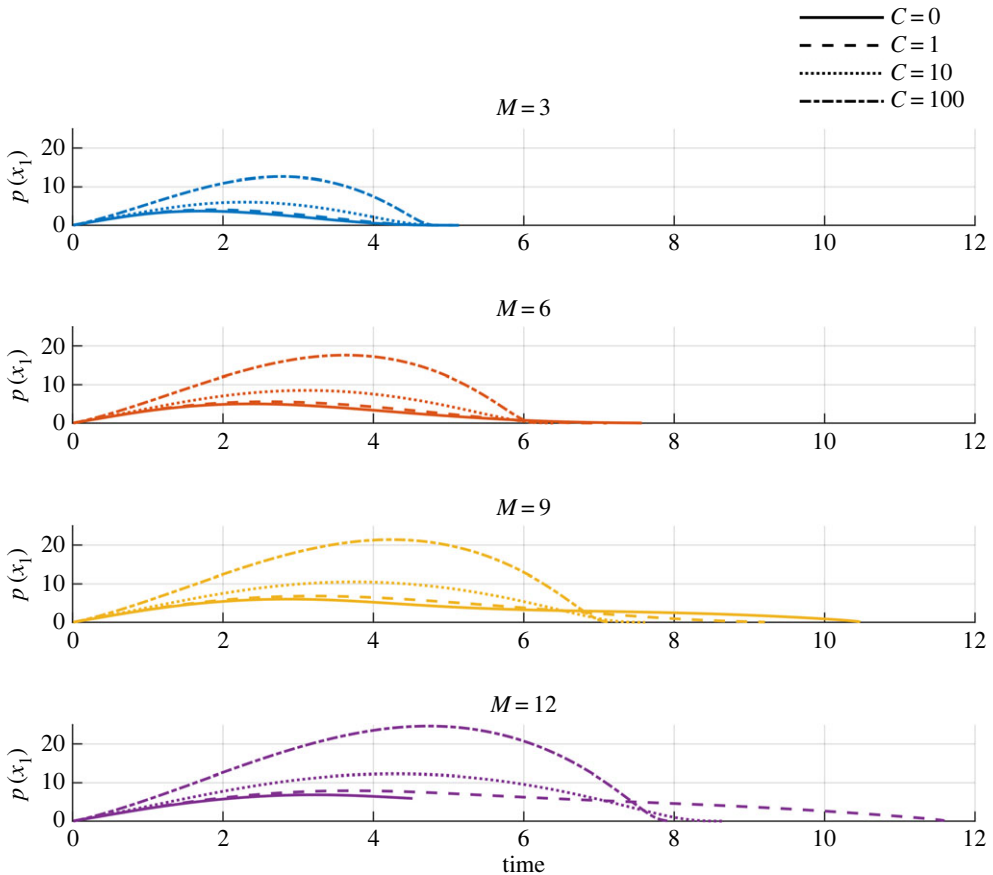
Figure 5. Evolution of the pressure on the body at the moving contact point x_1 as a function of scaled time for varying $M = 3I$, $I = 1, 2, 3, 4$, and varying $C = 0, 1, 10, 100$. See table 1 for all parameter values. (Online version in colour.)

(iv) Suppression of body rotation

In each of the cases presented in figure 4, an initial anti-clockwise moment on the body causes the body's angular velocity to increase and thus decrease its angle of inclination. For most cases, this trend continues throughout the skimming motion until near to the body's exit. However, when C is small, and M and I are comparatively large, there is a reversal in the body's rotation that increases its inclination. This is a consequence of the heavy body resisting the rotational torque which, in part, enables the super-elastic responses for heavier cases (i.e. the body remains in contact with the water layer for longer, maintaining higher positive pressure under the body which in turn leads to the super-elastic response). Once again, however, larger body curvature works to inhibit the effects of larger mass such that the body behaves similarly to a flat plate with no reversal in the rotational dynamics.

(v) Reduction of wake effects

The water layer velocity and free-surface height perturbations in the wake of the body (2.4a), (2.4b) are presented for successful skims in figures 6 and 7, respectively. The profiles show the characteristics of the developed wake of each case addressed above close to body exit, i.e. at a time $t_e - 0.5$, where t_e is the time of body exit. When the body's mass increases (relative to body curvature), the wake's profile is stretched in the positive x-direction (downstream). Additionally, larger mass produces a marginal increase in the velocity of the free-surface and a significant increase in the height of the free-surface aft of the body. When C is increased, the
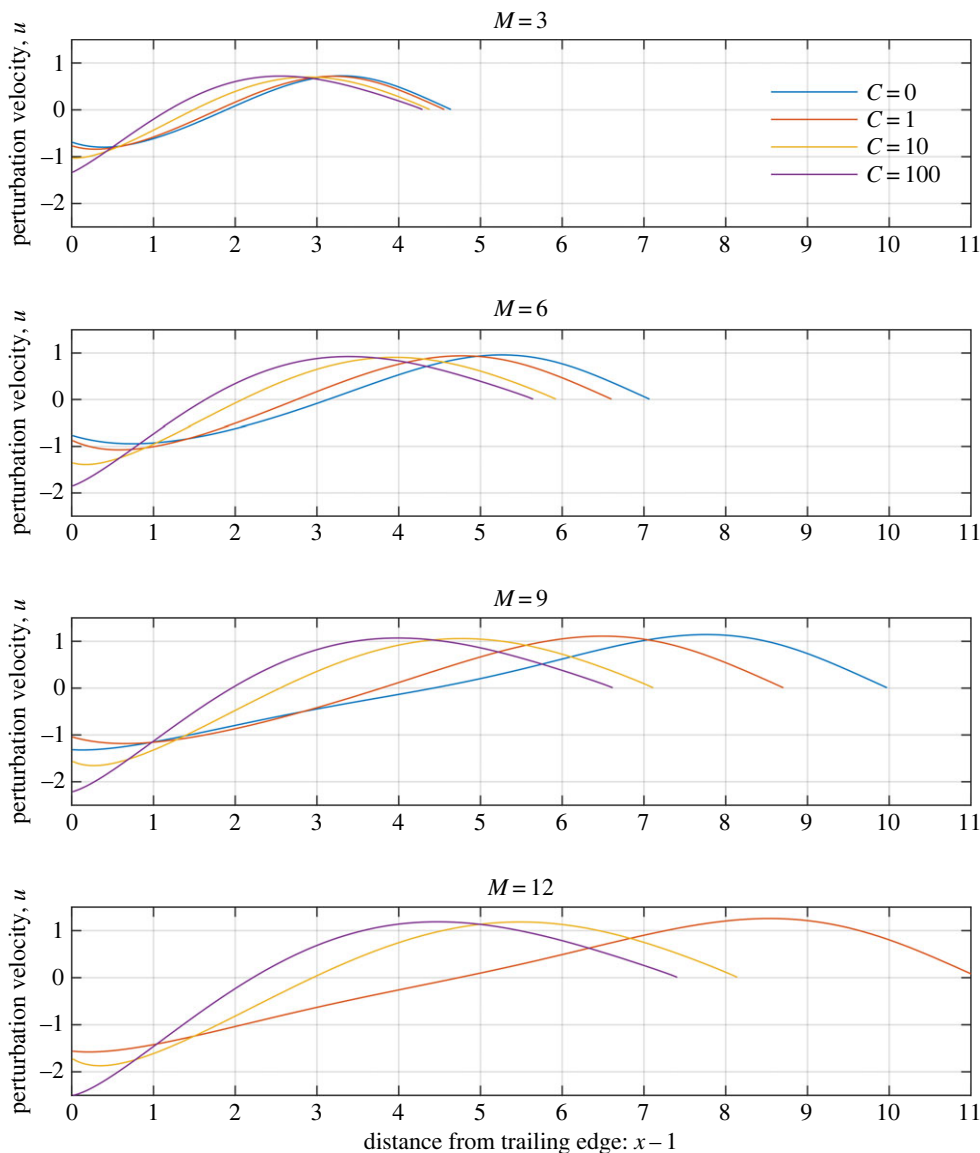
Figure 6. Profiles of the perturbation velocity in the wake of the body at distances from the trailing edge ($x = 1$). Plots show the results for varying $M = 3I$, $I = 1, 2, 3, 4$, and varying $C = 0, 1, 10, 100$. See table 1 for all parameter values. (The profile for $M = 12$ and $C = 0$ is omitted due to flooding.). (Online version in colour.)

wake effects are reduced in the x-direction yet remain of a similar order of magnitude (although interestingly, larger negative perturbation velocities are seen close to the body's trailing edge). Thus, approximately, the body's mass influences the free-surface height and velocity and the overall magnitude of the wake's length, while the body's curvature modulates the extent to which these effects persist aft of the body (for a given body mass).

4. Analysis for large mass and large curvature

The emphasis now is placed on analysing the skimming system when M, I, C are all increased and then on identifying the vital relationship between C, M for skimming to succeed, with I kept proportional to M throughout. As shown above, by increasing the body's mass and inertia relative
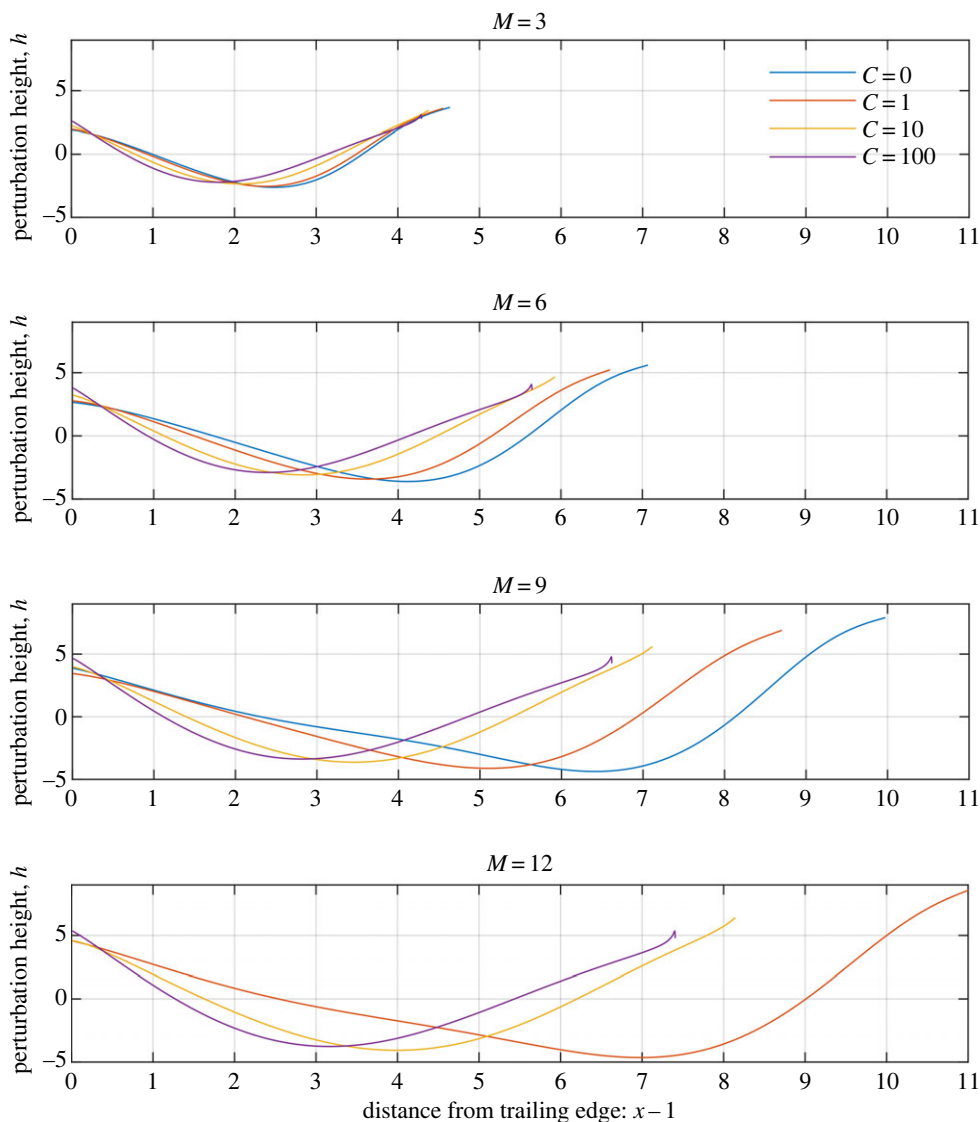
Figure 7. Profiles of the free-surface perturbation height in the wake of the body at distances from the trailing edge ($x = 1$). Plots show the results for varying $M = 3I$, $I = 1, 2, 3, 4$, and varying $C = 0, 1, 10, 100$. See table 1 for all parameter values. (The profile for $M = 12$ and $C = 0$ is omitted due to flooding.). (Online version in colour.)

to its curvature, the duration of the skim increases and flooding becomes more likely, while in some cases a super-elastic response is possible. Yet, with increased C the depth of the body's penetration diminishes and the time to exit shortens. The competing effects of large M and I and increased C are considered in detail below, returning to the original interaction equations of §2. This applies for a general smooth shape of the underbody T and it is found possible to determine the contact position $x_1(t)$ more analytically here as well as identifying the balance $C \sim M^{2/3}$ as a distinguished scaling. There are three temporal stages as described in (a–c).

(a) Stage 1: water entry

The first stage, soon after entry, follows [10] exactly since M and I play no significant role within the entry stage. To summarize the salient points here, for small time, the body has just entered

the liquid layer; hence the leading contact point and trailing edge of the body nearly coincide. As a result, there is a small spatial scale for body wetting near the entry point $x - 1 = C^{-1}x^*$ (as indicated by the orders of magnitude) with x^* of $O(1)$. A distinguishing feature of this first stage is the comparability between horizontal body speed and wetting speed and thus time scales as $t = C^{-1}t^*$ (corresponding to the contact speed being of order unity). Additionally, the underbody function T is small and $O(C^{-1})$. Given the small length and time scales the effects of increased mass and moment of inertia are delayed until the next stage of the skimming motion. Furthermore, since the initial body velocity is $O(1)$ and the body surface is highly curved, we expect the variations in u, p, h, Y, θ to all be $O(C^{-1})$.

Expanding the variables with respect to these scales and substituting into the equations of motion leads to a single nonlinear ODE (the workings of which are found in [10])

$$(\tau - V^{**}t^*)\chi\chi'' + \{\chi\tau' - 2V^{**}\chi + (\tau - V^{**}t^*)(\chi' - 2)\}\chi' + 2V^{**}\chi = V^{**}t^*, \tag{4.1a}$$

where $\chi(t^*) = x_1^*(t^*)$, $\tau(t^*) = sx^* + qx^{*2}$ is the scaled underbody shape with s and q both $O(1)$ constants, and $V^{**} = V_0^* + \omega_0^*$ is a constant comprised of the scaled vertical velocity and scaled angular velocity. Also here $x_1 = 1 + C^{-1}x_1^*$. The response at large t^* shows the growth

$$x_1^* \sim \lambda t^{*2/3} + \cdots, \quad f_1^* \sim \mu t^* + \cdots, \quad (t^* \to \infty), \tag{4.1b}$$

where $\lambda = -(3V^{**}/(4q))^{1/3}$, $\mu = 2q\lambda^3/3$. In addition, the other properties act according to

$$(u^*, p^*, h^*, T^*) \sim q\lambda^2(1, -1, -1, 1)t^{*4/3} + O(t^*). \tag{4.1c}$$

Altogether, the large t^* behaviour here informs the onset of the next stage, the majority of the skimming motion, in which we see new dynamics owing to the large curvature and increased mass.

(b) Stage 2: the majority of the skimming motion

The second stage explains the majority of the skimming motion featuring the body's downward and upward movement through the water layer (if a successful rebound occurs). In contrast to stage 1, the lift and moment on the body are now significant as the time t now rises to $O(1)$. We first summarize the $M \sim 1$ findings in [10]. The key results for M of order unity, deduced from (4.1b), (4.1c), are that the spatial scale here is $x - 1 = C^{-1/3}X$ with X of $O(1)$ and the expansion of the solution along with the underbody shape takes the form

$$x_1(t) - 1 = C^{-1/3}X_1(t) + C^{-2/3}X_{11}(t) + \cdots, \tag{4.2a}$$

$$(p, h, u, T - C^{2/3}\sigma_1 X) = C^{1/3}(\bar{p}_0, \bar{h}_0, \bar{u}_0, \bar{T}_0) + (\bar{p}_1, \bar{h}_1, \bar{u}_1, \bar{T}_1) + \cdots \tag{4.2b}$$

and $$(Y, \theta) = (C\sigma_2 + \bar{Y}_0, C\sigma_1 + \bar{\theta}_0) + \cdots. \tag{4.2c}$$

Substituting these expansions into (2.2) and (2.3) and working through, it can shown that the body's progression through the liquid layer can be determined by a linear ODE

$$Z''' = -c_1 Z, \tag{4.3a}$$

where $Z = X_1^3$ and $c_1 = (I + M)/(2IM)$ is a positive constant. Of note, this ODE is formulated using a local underbody shape correction of $\bar{T}_0(X) = qX^2$. The initial condition must match the trend (4.1b) from the first stage such that

$$Z \sim \lambda^3 t^2 \quad \text{as } t \to 0^+, \tag{4.3b}$$

with $\lambda^3 = -3V^{**}/(4q)$ being negative.

For increased-mass effects, we consider (4.3a) when the mass M becomes large; then the constant $c_1 \sim 1/M$ which implies that the time scale increases like $M^{1/3}$. Furthermore, the initial condition (4.3b) continues to hold over a large portion of time since the influence of the right-hand side of (4.3a) is delayed, suggesting that Z becomes of order $M^{2/3}$ and thus X_1 grows as $M^{2/9}$. This

correction term then overtakes the dominant term in (4.2a) when M is as large as $C^{3/2}$, providing the new feature of interest here when mass is large.

Therefore, we deduce, and highlight, the scaling

$$C = M^{2/3}C^*,$$

with C^* of $O(1)$ as the new setting of the present analysis. This leads to a new distinguished time scale of $O(M^{1/3})$ which brings in the lift and moment significantly. These arguments then imply the following scales and expansions:

$$x_1(t) - 1 = O(1), \quad x_1' = M^{-1/3}\frac{dx_1}{dt^*}, \tag{4.4a}$$

$$(p, h, u, T) = M^{2/3}(p_0, h_0, u_0, T_0) + M^{1/3}(p_1, h_1, u_1, T_1) + \cdots \tag{4.4b}$$

and

$$(Y, \theta) = M^{2/3}C^*(\sigma_2, \sigma_1) + M^{1/3}(Y_0(t^*), \theta_0(t^*)) + \cdots. \tag{4.4c}$$

Notably, the initial conditions require $\sigma_1 + \sigma_2 = 0$ and according to (4.4a) the underbody is wetted substantially. Substitution of (4.4a)–(4.4c) into (2.2) and (2.3) gives the balances

$$\frac{Y_0''(t^*)}{C^*\sigma_2} = \frac{1}{2}(1 - x_{10}(t^*))^2 - \frac{1}{C^*\sigma_2}\int_{x_{10}}^1 T_0(x)\,dx, \tag{4.5a}$$

$$\frac{I^*\theta_0''(t^*)}{C^*\sigma_2} = \frac{1}{6}(1 - x_{10}(t^*))^2(2x_{10}(t^*) + 1) - \frac{1}{C^*\sigma_2}\int_{x_{10}}^1 xT_0(x)\,dx \tag{4.5b}$$

and

$$\frac{Y_0(t^*) + \theta_0(t^*)}{C^*\sigma_2} = 2x_{10}'(t^*)\left((1 - x_{10}(t^*)) - \frac{1}{C^*\sigma_2}T_0(x_{10}(t^*))\right), \tag{4.5c}$$

where x_{10} comes from the expansion of $x_1 = x_{10} + M^{-1/3}x_{11} + \cdots$. Thus, the motion of the body during this stage reduces to the above nonlinear system of equations.

The initial conditions at small time t^* follow from (4.3b) or from (4.1b) and (4.1c) to give

$$x_{10}(t^*) \sim 1 - \lambda^* t^{*2/3}, \tag{4.6a}$$

$$Y_0(t^*) \sim V_0 t^* \tag{4.6b}$$

and

$$\theta_0(t^*) \sim \omega_0 t^*, \tag{4.6c}$$

as $t^* \to 0_+$, with $\lambda = (3(V_0 + \omega_0)/(2d^2 T_0/dx^2(1)))^{1/3}$ being a positive constant.

The form (4.5a)–(4.5c) holds for a general shape $T_0(x)$. Solutions for $T_0 = (1 - x^2)$ with $V_0(0) = -1$, $\omega_0(0) = 0$, $\sigma_1 = -\sigma_2 = -2$, $I = 10, 100, 1000$, $M = 3I$ and $C^* = 5$ and 1000 are shown in figure 8. Overall, closer agreement is seen between the asymptotic solutions (4.5a)–(4.5c) and the numerical calculations of the full system (2.1)–(2.6) during the portion of the skim when the body is descending into the liquid layer, and matches more closely towards the exit when the body mass is larger or x_1 remains small overall (i.e. when C^* is large). In figure 8a, the scaled leading edge position of the wetted region is presented. For smaller values of C^*, e.g. $C^* = 5$, we see x_1 tends closer to -1 (the leading edge of the solid body) and the duration of the skim increases. When C^* increases in magnitude the large curvature dynamics of [10] begin to dominate with the exit time tending towards a limit and with x_1 remaining close to 1.

These trends are further confirmed by figure 8b,c where the vertical movement of the body and its rotational dynamics are shown, respectively. In particular, for $C^* = 5$, the exit height and velocity are far greater in comparison to those for larger values C^*, with the super elastic response of a heavy body possible for smaller values of C^* still. Additionally, the large mass rotational dynamics are also seen with the body rotating more slowly and potentially reversing (which occurs for $C^* < 1$). When C^* increases, the curves for Y_0, V_0, θ_0 and ω_0 each tend to a limit, confirming the large curvature dynamics.
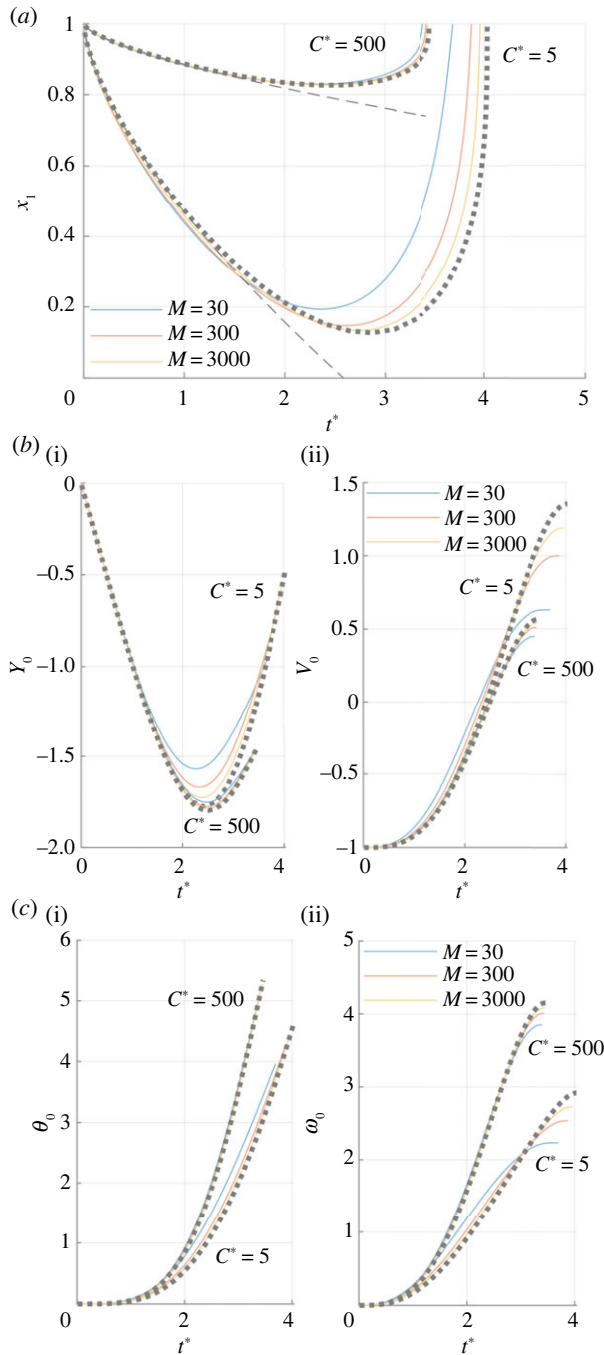
Figure 8. Examples showing agreement between the asymptotic and full solutions against scaled time $t^* = M^{-1/3}t$ for $M = 3I$ with $I = 10, 100, 1000$. All other parameters values match those in table 1. In each case, the asymptotic solution matches most closely as the body descends into the liquid layer and when x_1 remains small overall (i.e. when C^* is large). (*a*) Comparison between the asymptotic solution for x_{10} using (4.5*a*)–(4.5*c*) (dashed black lines) and the full solution for x_1 using (2.1)–(2.6) for $C^* = 5$ and $C^* = 500$ (labelled). (*b*) Comparison between the asymptotic solutions for Y_0 (i) and V_0 (ii) using (4.5*a*)–(4.5*c*) (dashed black lines) and the full solution for Y (i) and V (ii) using (2.1)–(2.6) for $C^* = 5$ and $C^* = 500$ (labelled). (*c*) Comparison between the asymptotic solutions for θ_0 (i) and ω_0 (ii) using (4.5*a*)–(4.5*c*) (dashed black lines) and the full solution for θ (i) and ω (ii) using (2.1)–(2.6) for $C^* = 5$ and $C^* = 500$ (labelled). (Online version in colour.)

The ending of stage 2 has the overall shape effects represented by T_0 becoming negligible since exit is approached; a square-root response arises in the contact point behaviour such that

$$x_1 \sim 1 - k(t_0^* - t^*)^{1/2} \quad \text{as } t^* \text{ tends to } t_{0-}^*, \tag{4.7}$$

as in the very recent work [28]. Here, k is a positive constant.

(c) Stage 3: Water exit

The final stage of the skim takes place over a short time scale t, deduced from the behaviour (4.7) to be of order $M^{-1/3}$ relative to the end value $M^{1/3}t_0^*$ found in the previous stage. The moving contact-point location takes the form

$$x_1 = 1 - O(M^{-1/3}). \tag{4.8}$$

This leads to the final exit process, with the underbody shape now having little effect. The time scale $M^{1/3}$ is consistent with the trend of the numerical results in figures 2–4 as M and I increase.

5. Conclusion

The skimming of a thin and heavy solid body following its oblique impact onto a water layer has been explored computationally and analytically using an inviscid spatially two-dimensional model with small-angle approximations. A special focus has been on understanding physically and quantifying the previously unexplored role of the underbody shape (represented by scaled curvature C) in combination with body mass (scaled as M) in determining the evolution of the contact point position at the front of the wetted area of the underbody. A crucial balance is seen to arise between C and $M^{2/3}$ in terms of orders of magnitude, that is

$$C \sim M^{2/3}. \tag{5.1}$$

Thus increased convex curvature of the underbody implies an increased likelihood that the skim will be successful. The time scales as $C^{1/2}$ for increasing curvature and mass. The balance between the curvature (shape) C and mass M therefore determines the dynamics seen during the skimming motion. Specifically, while large mass leads to deeper, longer skimming motions, larger wake effects that extend further aft, and the potential for a super elastic response, when curvature is increased these effects are much inhibited and indeed shortened (mainly due to the underbody shape qualitatively and quantitatively changing the pressure response under the body). The precise conditions at entry also play a part while body weight ($M\mathbf{g}$), largely negligible during the skim, matters during any flight through air between successive skims. The study here which covers all smooth shapes of body in principle shows that shape is an important influence in the early and middle phases of a successful skim but less significant during the final exit phase as the body rebounds from the water.

A major finding is that for any mass of particle there is a critical value of the underbody curvature that would produce maximal wetting; for curvatures above the critical value a body will successfully skim for the given initial conditions. Further, the occurrence of a super-elastic response in the exit vertical velocity and in the corresponding height of the body is inhibited when curvature is suitably increased. This is in addition to the specific scales identified in the previous paragraph.

The physical understanding and prediction of skims for bodies that are, in a sense, both fatter and heavier than previously addressed may prove helpful for future direct numerical studies. The small-perturbation approach in the current paper, while nonlinear, is more analytical with formulaic results and is often quite realistic in covering wide parameter ranges. The moving contact point is determined fairly readily by this method whereas it can be a difficult property to pin down in direct computational approaches, for example. The analysis also enables the question raised in the introduction concerning successful heavier-body skims to be given an affirmative answer.

The particular novelty of this study lies in the consideration and interplay of body thickness and convex curvature or underbody shaping of the body with increased mass. These factors lead to new asymptotic results that show the dominant underlying physics at different stages of the skimming motion. Therefore, the presented analysis is distinct from previous studies in which flat bodies are of concern [8,28] and those in which underbody shape varies but with smaller mass [10]. The above considerations thus tend to make the modelling more physically realistic than before. The combined influence of body shape and mass is potentially important: for instance (5.1) implies that a body whose mass or weight is increased by a factor of 8 say can still skim successfully provided its convex curvature is raised by a factor of 4. It would be helpful to also extend the modelling to allow for three spatial dimensions, including the influence of spin about the vertical axis which appears to be central for the air flights between skims. There are other physical effects neglected here that are present in real applications to varying degrees of significance: air effects may be among the most notable in certain circumstances.

Several points are of much potential interest to the applications mentioned in the introduction, especially to industry. For instance, the work shows a range of skimming motions which could be relevant in the aircraft icing context. First, flooding and sinking can lead to ice growth in a liquid layer. Second, for different bodies, completed skims generate a range of post-skim trajectories depending on curvature and mass. Given a relatively consistent range of ice particle densities, continued analysis could match parameter ranges to what dynamics may be seen (e.g. concerning when super-elastic rebounds may occur). Usually the rather 'erratic' response of skimming particles makes their post-skim trajectories very hard to predict. Future modelling could also address post-ejection trajectories with rotational dynamics/multiple skims, leading perhaps to very interesting re-entry orientations and initial conditions. Third, the super-elastic response is of much interest as regards the interaction with oncoming air flow in practice and the possibility of destabilization of the air flight. Fourth, a wider range of shapes ideally needs to be considered, including a relaxing of the sharp trailing edge assumption (see [12,13]).

Appendix A. Comment on the numerical methods and solutions

The results presented in figures 2–8 were computed in MATLAB R2020b on a computer with a 2.60 GHz Intel(R) Core(TM) i7-9850H processor and 16 GB of RAM. The system of equations solved is presented in (2.1)–(2.6), and forms six ODEs and four linear equations that are solved simultaneously at each time step. To verify the code, initial computations were performed to replicate and compare with the solutions presented in Hicks & Smith [8]. Furthermore, our comparisons between the numerical results for the full system and the asymptotic solutions developed within the current paper (and the preceding papers [10,28]) provide further verification of the modelling.

As the body enters or exits the liquid layer, x_1 is near to the trailing edge at $x = 1$. The numerical solutions are particularly sensitive here, requiring an accurate small-time solution (presented in

Table 2. The typical runtimes of analysis presented in figures 2–5 in seconds for skimming motions of varying mass and scaled underbody curvature.

runtime in seconds	$C = 0$	$C = 1$	$C = 10$	$C = 100$
$M = 3$	0.4375	1.9460	3.7786	5.1647
$M = 6$	0.8517	2.2895	4.1036	5.4828
$M = 9$	1.3992	2.8425	4.4851	5.8387
$M = 12$	1.6251	3.5418	4.9271	6.2381

Table 3. Maximum percentage errors for x_1 comparing the solutions for computations using an adaptive time step method with those using a fixed, higher resolution time step method.

maximum x_1 error	$C = 0$ (%)	$C = 1$ (%)	$C = 10$ (%)	$C = 100$ (%)
$M = 3$	0.1441	0.0881	0.0209	0.0101
$M = 6$	0.0863	0.0577	0.0233	0.0156
$M = 9$	0.5363	0.3269	0.0287	0.0290
$M = 12$	0.0177	0.5132	0.0456	0.0108

Table 4. Maximum percentage errors for Y comparing the solutions for computations using an adaptive time step method with those using a fixed, higher resolution time step method.

maximum Y error	$C = 0$ (%)	$C = 1$ (%)	$C = 10$ (%)	$C = 100$ (%)
$M = 3$	0.0130	0.0089	0.0020	0.0002
$M = 6$	0.0241	0.0120	0.0024	0.0003
$M = 9$	0.0345	0.0166	0.0031	0.0003
$M = 12$	0.0156	0.0269	0.0035	0.0004

[10]) and an accurate ODE solver. To this end, we employed a seventh/eighth-order Runge–Kutta method with adaptive time stepping using a minimum time-step size of 10^{-6} and a maximum size of 10^{-2}. The spatial error tolerances are set at 10^{-6}, which is used to determine when time step needs to be changed for increased accuracy or improved runtime. Of note, parallelization was not used since the typical runtimes last only a few seconds (stated below).

Firstly, we show the running time for the analyses presented in figures 2–5. Sixteen examples of skimming motion are shown in these figures, for increasing mass values of $M = 3, 6, 9$ and 12, and scaled body curvature of $C = 0, 1, 10, 100$. In each case, the code is reasonably fast due to the adaptive time stepping increasing the step size when appropriate. The values included in table 2 are from a single run of the code and represent the typical runtime of our analysis. Of interest, the time steps for the computation near entry and exit are calculated to be $O(10^{-6})$, while for the majority of the skimming motion they are $O(10^{-2})$, reflecting the greater need for accuracy when x_1 is close to the trailing edge.

Secondly, we present the percentage error for the data presented in figures 2–5 (produced using an adaptive time-step method as detailed above) compared with solutions using a fixed time step of size 10^{-6} throughout (notably, smaller timesteps result in unreasonable run times with no benefit in incremental accuracy). In tables 3–7, we present the maximum percentage errors across the whole solution of each as a percentage difference of the refined solution.

Table 5. Maximum percentage errors for V comparing the solutions for computations using an adaptive time step method with those using a fixed, higher resolution time step method.

maximum V error	$C = 0$ (%)	$C = 1$ (%)	$C = 10$ (%)	$C = 100$ (%)
$M = 3$	0.0099	0.0057	0.0010	0.0001
$M = 6$	0.0202	0.0078	0.0011	0.0001
$M = 9$	0.0317	0.0111	0.0013	0.0001
$M = 12$	0.0160	0.0163	0.0014	0.0001

Table 6. Maximum percentage errors for θ comparing the solutions for computations using an adaptive time step method with those using a fixed, higher resolution time step method.

maximum θ error	$C = 0$ (%)	$C = 1$ (%)	$C = 10$ (%)	$C = 100$ (%)
$M = 3$	0.0276	0.0166	0.0043	0.0007
$M = 6$	0.0288	0.0153	0.0051	0.0008
$M = 9$	0.0273	0.0144	0.0055	0.0010
$M = 12$	0.0092	0.0152	0.0057	0.0011

Table 7. Maximum percentage errors for ω comparing the solutions for computations using an adaptive time step method with those using a fixed, higher resolution time step method.

maximum ω error	$C = 0$ (%)	$C = 1$ (%)	$C = 10$ (%)	$C = 100$ (%)
$M = 3$	0.0107	0.0070	0.0017	0.0002
$M = 6$	0.0118	0.0060	0.0014	0.0002
$M = 9$	0.0206	0.0058	0.0014	0.0002
$M = 12$	0.0154	0.0101	0.0013	0.0002

References

1. Gent R, Dart N, Cansdale J. 2000 Aircraft icing. *Phil. Trans. R. Soc. A* **358**, 2873–2911. (doi:10.1098/rsta.2000.0689)
2. Mason J, Strapp W, Chow P. 2006 The ice particle threat to engines in flight. In *44th AIAA Aerospace Sciences Meeting and Exhibit, Reno, NV, 9–12 January 2006*, p. 206. Reston, VA: AIAA.
3. Purvis R, Smith F. 2016 Improving aircraft safety in icing conditions. In *UK Success Stories in Industrial Mathematics*, pp. 145–151, Cham: Springer.
4. Smith F, Balta S, Liu K, Johnson ER. 2019 On dynamic interactions between body motion and fluid motion. In *Mathematics Applied to Engineering, Modelling, and Social Issues*, pp. 45–89, New York, NY: Springer.
5. Von Kàrmàn T. 1929 The impact of seaplanes floats during landing. NACA, TN(321).
6. Wagner H. 1931 Landing of seaplanes. NACA, TN(622).
7. Edge R. 1968 The surf skimmer. *Am. J. Phys.* **36**, 630–631. (doi:10.1119/1.1975037)
8. Hicks P, Smith F. 2010 Skimming impacts and rebounds on shallow liquid layers. *Proc. R. Soc. A* **467**, 653–674. (doi:10.1098/rspa.2010.0303)
9. Liu K, Smith F. 2014 Collisions, rebounds and skimming. *Phil. Trans. R. Soc. A* **372**, 20130351. (doi:10.1098/rsta.2013.0351)
10. Palmer R, Smith F. 2020 Skimming impacts and rebounds of smoothly shaped bodies on shallow liquid layers. *J. Eng. Maths* **124**, 41–73. (doi:10.1007/s10665-020-10063-6)
11. Tuck E, Dixon A. 1989 Surf-skimmer planing hydrodynamics. *J. Fluid Mech.* **205**, 581–592. (doi:10.1017/S0022112089002168)

12. Khabakhpasheva T, Korobkin A. 2013 Oblique impact of a smooth body on a thin layer of inviscid liquid. *Proc. R. Soc. A* **469**, 20120615. (doi:10.1098/rspa.2012.0615)
13. Liu K, Smith F. 2021 A smoothly curved body skimming on shallow water. *J. Eng. Maths* **128**, 17. (doi:10.1007/s10665-021-10130-6)
14. Wagner H. 1932 Über stoß-und gleitvorgänge an der oberfläche von flüssigkeiten. *ZAMM–J. Appl. Math. Mech./Zeitschrift für Ange. Math. und Mechanik* **12**, 193–215. (doi:10.1002/zamm.19320120402)
15. Green A. 1935 The gliding of a plate on a stream of finite depth. *Proc. Camb. Phil. Soc.* **31**, 589–603. (doi:10.1017/S0305004100013591)
16. Green A. 1936 The gliding of a plate on a stream of finite depth. Part II. *Proc. Camb. Phil. Soc.* **32**, 67–85. (doi:10.1017/S0305004100018867)
17. Watanabe I. 1986 Analytical expression of hydrodynamic impact pressure by matched asymptotic expansion technique. In *Transactions of the West-Japan Society of Naval Architects 71:77–85*, The Japan Society of Naval Architects and Ocean Engineers.
18. Cointe R, Armand J. 1987 Hydrodynamic impact analysis of a cylinder. *ASME J. Offshore Mech. Arct. Eng.* **109**, 237–243. (doi:10.1115/1.3257015)
19. Greenhow M. 1987 Wedge entry into initially calm water. *Appl. Ocean Res.* **9**, 214–223. (doi:10.1016/0141-1187(87)90003-4)
20. Greenhow M. 1988 Water-entry and-exit of a horizontal circular cylinder. *Appl. Ocean Res.* **10**, 191–198. (doi:10.1016/S0141-1187(88)80003-8)
21. Scolan Y, Korobkin A. 2001 Three-dimensional theory of water impact. Part 1. Inverse Wagner problem. *J. Fluid Mech.* **440**, 293–326. (doi:10.1017/S002211200100475X)
22. Korobkin A. 2004 Analytical models of water impact. *Eur. J. Appl. Math.* **15**, 821–838. (doi:10.1017/S0956792504005765)
23. Howison S, Ockendon J, Oliver J. 2004 Oblique slamming, planing and skimming. *J. Eng. Math.* **48**, 321–337. (doi:10.1023/B:engi.0000018156.40420.50)
24. Hewitt I, Balmforth N, McElwaine J. 2011 Continual skipping on water. *J. Fluid Mech.* **669**, 328–353. (doi:10.1017/S0022112010005057)
25. Lee D-G, Kim H-Y. 2008 Impact of a superhydrophobic sphere onto water. *Langmuir* **24**, 142–145. (doi:10.1021/la702437c)
26. Gilet T, Bush JW. 2012 Droplets bouncing on a wet, inclined surface. *Phys. Fluids* **24**, 122103. (doi:10.1063/1.4771605)
27. Galeano-Rios CA, Cimpeanu R, Bauman IA, MacEwen A, Milewski PA, Harris DM. 2021 Capillary-scale solid rebounds: experiments, modelling and simulations. *J. Fluid Mech.* **912**, A17. (doi:10.1017/jfm.2020.1135)
28. Palmer RA, Smith FT. 2022 Skimming impact of a thin heavy body on a shallow liquid layer. *J. Fluid Mech.* **940**, A6. (doi:10.1017/jfm.2022.207)
29. Smith F, Li L, Wu G. 2003 Air cushioning with a lubrication/inviscid balance. *J. Fluid Mech.* **482**, 291–318. (doi:10.1017/S0022112003004063)
30. Hicks PD, Purvis R. 2013 Liquid–solid impacts with compressible gas cushioning. *J. Fluid Mech.* **735**, 120–149. (doi:10.1017/jfm.2013.487)
31. Henman NI, Smith FT, Tiwari MK. 2021 Pre-impact dynamics of a droplet impinging on a deformable surface. *Phys. Fluids* **33**, 092119. (doi:10.1063/5.0064626)
32. Moore MR. 2021 Introducing pre-impact air-cushioning effects into the wagner model of impact theory. *J. Eng. Math.* **129**, 1–23. (doi:10.1007/s10665-021-10137-z)
33. Fehlberg E. 1968 Classical fifth-, sixth-, seventh-, and eighth-order Runge-Kutta formulas with stepsize control.
34. M. Compere. 2001 "ode78.m, v1.14": (https://gitlab.com/comperem/ode_solvers)
35. Smith F, Liu K. 2017 Flooding and sinking of an originally skimming body. *J. Eng. Maths* **107**, 37–60. (doi:10.1007/s10665-017-9925-7)
36. Palmer RA, Smith FT. 2023 The role of body shape and mass in skimming on water. Figshare. (doi:10.6084/m9.figshare.c.6350478)